INFLUENCE OF IMPELLER SHROUD FORCES ON TURBOPUMP ROTOR DYNAMICS

Jim P. Williams
Bell Helicopter Textron, Inc.
Group 06, Dept. 81, MS 14
Fort Worth, Texas 76101, U.S.A.

Dara W. Childs
Department of Mechanical Engineering
Texas A&M University
College Station, Texas 77843, U.S.A.

The shrouded-impeller leakage path forces calculated by Childs (1987) have been analyzed to answer two questions. First, because of certain characteristics of the results of Childs, the forces could not be modeled with traditional approaches. Therefore, an approach has been devised to include the forces in conventional rotordynamic analyses. The forces were approximated by traditional stiffness, damping and inertia coefficients with the addition of whirl-frequency-dependent direct and cross-coupled stiffness terms. The forces were found to be well-modeled with this approach. Finally, the effect these forces had on a simple rotor-bearing system was analyzed, and, therefore, they, in addition to seal forces, were applied to a Jeffcott rotor. The traditional methods of dynamic system analysis were modified to incorporate the impeller forces and yielded results for the eigenproblem, frequency response, critical speed, transient response and an iterative technique for finding the frequency of free vibration as well as system stability. All results lead to the conclusion that the forces have little influence on natural frequency but can have appreciable effects on system stability. Specifically, at higher values of fluid swirl at the leakage path entrance, relative stability is reduced. The only unexpected response characteristics that occurred are attributed to the nonlinearity of the model.

INTRODUCTION

The vibration of centrifugal pumps has received increasing attention recently because of the inability of current analysis techniques to adequately predict the dynamic characteristics of pump designs. Failure to accurately predict vibrations has resulted in the loss of considerable amounts of money in down time from severe vibration problems. Massey (1985), for example, described an eleven-stage pump that became unstable when its running speed exceeded its critical speed by 25%. In other words, it whirled at 80% of running speed. Another example occurred in the High Pressure Oxygen Turbopump (HPOTP) of the Space Shuttle Main Engine (SSME) which also whirled at 80% of running speed (Childs and Moyer, 1985).

The hydrodynamic forces generated in many of the fluid-filled gaps within the pump are well-established contributors to the problems cited above. This article is concerned specifically with the forces developed along the leakage path between the impeller and the shroud, as shown in Figure 1. As the fluid is discharged from the impeller, some will return to the lower-pressure, suction side by way of this leakage path. Leakage is minimized typically with wear ring seals, as shown. Hydrodynamic forces are developed along the entire leakage path, i.e. the shroud section as well as the seal. Note

that these are only parts of the total force on the impeller and that the impeller/volute region, balance drums, inducers, shaft, etc. also contribute to the dynamics of pumps, although they are not considered here.

Unfortunately, measurements of the total force on actual impellers have typically been obtained using pumps that have been modified to minimize leakage path forces. However, some results have been reported that are of importance here. For example, research at Cal Tech (Adtkins, 1976) led to the conclusion that the pressures in the shroud annulus contributed from about 50% to 75% of the total stiffness acting on the impeller. The pump used included separation rings and an enlarged shroud clearance space to minimize leakage flow forces.

Bolleter et al. (1985) used a rocking-arm mechanism to vertically translate the spinning impeller. Their pump had normal clearances in the leakage path; and, therefore, the forces measured were more realistic. The results demonstrated that the nondimensionalized cross-coupled stiffness value was about twice that measured on the pump at Cal Tech (Jery et al., 1984). This suggests that the leakage path region in pumps can also reduce the stability of impeller motion.

Almost all of the analytical attempts at predicting leakage path forces have been concerned with seals. However, Childs has extended his previous techniques in seal analysis (1980, 81, 82a, 82b, 82c) to apply them to the flow within the clearance space surrounding the shroud (1987). His work will be used to model the seal and shroud forces in this article and will now be summarized.

Childs used a bulk-flow approach to obtain the governing equations of the flow of a differential element of fluid. In the seal problem, three equations were required: axial- and circumferential-momentum equations as well as the continuity equation. In the shroud problem, the axial-momentum equation was replaced by a path-momentum equation, introducing additional terms which described the centrifugal and Coriolis accelerations of the fluid element. After a perturbation expansion of the equations in the eccentricity ratio, the resulting relationships were solved at various values of the whirl frequency, Ω. Integration of the resulting pressure distribution on the shaft or shroud yielded the radial and tangential force as functions of whirl frequency. In addition, solution was carried out at various circumferential velocities at the shroud entrance. This variable is of primary importance in system stability (cross-coupled stiffness). Figure 2 shows the results of the shroud problem for three different values of the inlet swirl velocity. The leakage path analyzed corresponded to that used by Bolleter et al. (1985) which ran at 2000 rpm. Figure 3 provides the dimensions of the pump and other data of importance.

In the articles cited above, Childs initially suggested the following conventional, linear relationship to model the forces. It applies for small motion of the rotor about the centered position.

$$-\begin{Bmatrix} F_x \\ F_y \end{Bmatrix} = \begin{bmatrix} M & 0 \\ 0 & M \end{bmatrix} \begin{Bmatrix} \ddot{x} \\ \ddot{y} \end{Bmatrix} + \begin{bmatrix} C & c \\ -c & C \end{bmatrix} \begin{Bmatrix} \dot{x} \\ \dot{y} \end{Bmatrix} + \begin{bmatrix} K & k \\ -k & K \end{bmatrix} \begin{Bmatrix} x \\ y \end{Bmatrix}. \tag{1}$$

If circular whirl at frequency, Ω, and radius, Q, is assumed such that

$$x = Q\cos\Omega t$$
$$y = Q\sin\Omega t, \tag{2}$$

the radial and tangential force components can be stated

$$-\begin{Bmatrix} F_r \\ F_t \end{Bmatrix} = Q \begin{Bmatrix} -M\Omega^2 + c\Omega + K \\ C\Omega - k \end{Bmatrix}. \tag{3}$$

After nondimensionalizing the terms as defined in (Childs, 1987), equations (3) become

$$\frac{\tilde{F}_r}{\tilde{q}} = \tilde{M}f^2 - \tilde{c}f - \tilde{K}$$
$$\frac{\tilde{F}_t}{\tilde{q}} = -\tilde{C}f + \tilde{k}, \tag{4}$$

where the definitions of the coefficients are included in the List of Symbols and the other variables are defined as follows.

$\tilde{F} = \dfrac{F}{2R_L L \Delta P}$, nondimensionalized force

$\tilde{q} = \dfrac{Q}{Q_o}$, nondimensionalized clearance

$f = \dfrac{\Omega}{\omega}$, whirl frequency ratio

$\dfrac{\tilde{F}}{\tilde{q}}$, force coefficient.

The quadratic relationships of equations (4) are to be used to obtain the dynamic coefficients of equations (1). Specifically, a least-squares curve fit of the force curves will yield the coefficients. This is an adequate approach for seal forces because they, in general, do follow a quadratic trend. However, the curves of Figure 2 illustrate that shroud forces can not be approximated by equations (4); and, therefore, a traditional linear model as expressed in equations (1) will not adequately represent the forces. Although these results are unexpected, experimental measurements made by Franz and Arndt (1986) of impellers with inducers yielded very similar results.

PROBLEM DEFINITION

At this point, it is not known, assuming the force curves of Figure 2 are valid, how they can best be included in traditional rotordynamic calculations of stability, response, critical speeds etc. To solve this problem, the present research has been conducted to answer the following questions.

1. How can the force curves found by Childs (1987) be incorporated in the traditional rotordynamic analyses of system response, stability, critical speeds etc.?

2. What effects do the forces have on a rotor-bearing system with respect to stability, natural frequencies, imbalance response, etc?

Before answering these questions, observe that the forces present no new problems in a transient analysis because they could be applied as whirl-frequency-dependent forcing functions to a simple rotor model such as that developed by Jeffcott (1919). The equations of motion would be nonlinear because the forces depend on the whirl frequency, defined kinematically as

$$f = \frac{\Omega}{\omega_s} = \frac{x\dot{y} - y\dot{x}}{\omega_s(x^2 + y^2)}, \tag{5}$$

but this could be handled by integrating the equations of motion numerically with traditional methods. However, a transient analysis alone is not sufficient to obtain an understanding of the forces, and this is why an answer to the questions posed above is necessary. The following section describes the model used to analyze the shroud forces, and results are then given for the eigenvalue problem and frequency response, respectively.

ROTORDYNAMIC MODEL

As shown in Figure 4, the model is a Jeffcott rotor (Jeffcott, 1919) under the application of seal and shroud forces. The rotor itself represents a double-suction impeller, yielding two symmetrical leakage paths. In summary, the forces on the rotor are the shaft stiffness, two identical seal forces and two identical shroud forces. The mathematical representation of each force will now be discussed.

A 90.7 kg (200 lb) rotor is assumed. In addition, the shaft stiffness used (K_{sh} = .2987 MN/m) makes the natural frequency of forward whirl (to be defined later) equal to 80% of shaft speed. This choice is not completely arbitrary since this frequency corresponds to that observed in the examples cited in the Introduction (Massey, 1985; Childs and Moyer, 1985).

The seals modeled are smooth, wear ring seals with a clearance and diameter of .36 mm and 236 mm, respectively. The least-squares approach of Childs described earlier has been carried out, and the resulting dynamic coefficients are given in Table 1. The analysis used under-predicts the true value of the direct stiffness coefficient which, therefore, is doubled later when the coefficients of the entire model are assembled.

Table 1. Coefficients for one wear ring seal.

$\tilde{u}_{tL}$ --	M_s kg	C_s Ns/m	c_s Ns/m	K_s MN/m	k_s MN/m
.5	.3111	3356.0	78.6	.6121	.4628
.6	.3398	2167.0	89.6	.5443	.4611
.7	.3714	970.9	101.3	.4755	.4455

As described in the Introduction, conventional stiffness, damping and mass coefficients can not completely describe the impeller-shroud forces calculated by Childs and shown in Figure 2. Therefore, the following method has been devised. First, a curve fit of the force curves is carried out, yielding dynamic coefficients which describe the quadratic variation of the forces with respect to the whirl frequency ratio as described above. The difference between these curve fits and the actual force curves is modeled by

direct and cross-coupled stiffness coefficients which are functions of whirl frequency ratio. The mathematical equivalent of this approach will now be discussed.

The following modified forms of equations (4) express the method with which the impeller-shroud forces are modeled.

$$\frac{\tilde{F}_r}{\tilde{q}} = \tilde{M}_L f^2 - \tilde{c}_L f - [\tilde{K}_L + \tilde{K}^*(f)]$$

$$\frac{\tilde{F}_t}{\tilde{q}} = - \tilde{C}_L f + [\tilde{k}_L + \tilde{k}^*(f)], \qquad (6)$$

where $\tilde{K}^*$ and $\tilde{k}^*$ represent the nondimensionalized deviations between the force curves and the approximating quadratic expressions. Figure 5 illustrates $\tilde{K}^*$ and $\tilde{k}^*$, respectively. Note that, although they represent forces proportional to displacement, they are not traditional stiffness coefficients since they are functions of whirl frequency ratio. In addition, because of the perturbation approach used by Childs, the original forces are linearly proportional to rotor displacement. This fact supports the usage of stiffness coefficients to model the forces in Figure 5. Equations (1) are now rewritten as

$$-\begin{Bmatrix} F_x \\ F_y \end{Bmatrix} = \begin{bmatrix} M_L & 0 \\ 0 & M_L \end{bmatrix} \begin{Bmatrix} \ddot{x} \\ \ddot{y} \end{Bmatrix} + \begin{bmatrix} C_L & c_L \\ -c_L & C_L \end{bmatrix} \begin{Bmatrix} \dot{x} \\ \dot{y} \end{Bmatrix} + \begin{bmatrix} K_L+K^*(f) & k_L+k^*(f) \\ -k_L-k^*(f) & K_L+K^*(f) \end{bmatrix} \begin{Bmatrix} x \\ y \end{Bmatrix}. \qquad (7)$$

Finally, observe that equations (7) are, in general, nonlinear differential equations. To understand this statement, recall that the general definition of the whirl frequency ratio, f, is given in equation (5). If the rotor precession has a constant radius and rate, f is a constant and the motion is linear. However, for general motion, f is variable and a function of the motion.

After performing the asymptotic least-squares curve fit to Figure 2, the resulting coefficients of equation (6) are given in Table 2.

Table 2. Approximating coefficients for one leakage path.

M_L kg	C_L Ns/m	c_L Ns/m	K_L MN/m	k_L MN/m
3.469	2037	969.9	.06781	.3137

Note that the above values apply for all three inlet tangential velocities to the leakage path. The frequency-dependent coefficients, $\tilde{K}^*$ and $\tilde{k}^*$, are illustrated in the curves of Figure 5.

In summary, the following equations represent how the overall coefficients for the model are defined.

$$M = M_r + 2(M_s + M_L)$$

$$C = 2(C_s + C_L) + \bar{C}$$

$$c = 2(c_s + c_L)$$

$$K = K_{sh} + 2(2K_s + K_L) + 2K^* = \bar{K} + 2K^*$$

$$k = 2(k_s + k_L) + 2k^* = \bar{k} + 2k^*. \tag{8}$$

Particular coefficients are doubled because there are two seals and two leakage paths in a double suction pump. The quantity, $\bar{C}$, must be added to the model to yield reasonable stability. If the eigenvalues of the overall system are obtained without adding $\bar{C}$, the system is found to be unstable. Therefore, by adding another damping term ($\bar{C}$ = 10,422 Ns/m), reasonable stability, which is consistent with operating pump experience, is ensured.

The following equation represents the complete model used to approximate the forces on the rotor.

$$\begin{bmatrix} M & 0 \\ 0 & M \end{bmatrix}\begin{Bmatrix} \ddot{x} \\ \ddot{y} \end{Bmatrix} + \begin{bmatrix} C & c \\ -c & C \end{bmatrix}\begin{Bmatrix} \dot{x} \\ \dot{y} \end{Bmatrix} + \begin{bmatrix} K(f) & k(f) \\ -k(f) & K(f) \end{bmatrix}\begin{Bmatrix} x \\ y \end{Bmatrix} = \begin{Bmatrix} F_x \\ F_y \end{Bmatrix}. \tag{9}$$

Table 3 contains the numerical values used for this analysis. These coefficients combine to make the damping for the uncoupled system, defined by $2\sqrt{\bar{K}M}$, equal to 63%, 59% and 54% of critical damping for the three swirl ratios shown, respectively. Again, $\tilde{K}^*$ and $\tilde{k}^*$ are illustrated in Figure 5 and are defined analytically with cubic-spline curve fits.

Table 3. Coefficients for overall model.

$\tilde{u}_{iL}$ --	M kg	C Ns/m	c Ns/m	$\bar{K}$ MN/m	$\bar{k}$ MN/m
.5	98.240	21208	2097.1	2.8827	1.5549
.6	98.298	18830	2119.1	2.6115	1.5494
.7	98.361	16438	2142.4	2.3363	1.5184

EIGENVALUE DETERMINATION AND INTERPRETATION

The characteristic equation for equation (9) is

$$(Ms^2 + Cs + K)^2 + (cs + k)^2 = 0. \tag{10}$$

Traditionally, the roots of the above quartic polynomial in the complex variable, s, are the system eigenvalues, the real part of which determines the stability while the imaginary part is the natural frequency. However, this description is not altogether complete as will be explained below. It can be shown that the four roots of equation (10) are two pairs of complex conjugates, corresponding to the forward whirl and backward whirl modes.

In solving equation (10) for the eigenvalues, there are of four roots for any whirl frequency ratio. Figures 6 and 7 show how only the forward-whirl eigenvalue varies with whirl frequency ratio for the three inlet swirl ratios.

The physical meaning of the eigenvalues is of interest, and Figure 7 will be used to explain this. In linear systems, the frequency of free vibration is determined by the imaginary part of the eigenvalues. However, this is not exactly true in the present whirl frequency-dependent model. Free whirl of the rotor occurs only when the imaginary part of an eigenvalue equals the whirl frequency. In Figure 7, therefore, only those points where the abscissa equals the ordinate can correspond to free vibration of the rotor. Further, stability is determined at the eigenvalue whose imaginary part equals the whirl frequency ratio.

To find this "natural frequency" and stability of free whirl, the following iterative technique has been used. First, a whirl frequency ratio is assumed. From this value, the corresponding values of K and k are obtained from the data shown in Figure 5 from which the eigenvalues are found using equation (10). These first two steps are equivalent to finding a point on the curves of Figure 6 and 7. The imaginary part of the forward-whirl eigenvalue is compared to the whirl frequency used. If they are the same, the natural frequency at which free vibration takes place is defined. If they are different, the imaginary part of the forward-whirl root becomes the assumed whirl frequency ratio, and the same steps are carried out until convergence occurs.

Tables 4 and 5 show results of the above algorithm. Also included are the eigenvalues of the same model neglecting K^* and k^*, which correspond to a pure quadratic approximation of the leakage path forces as in equations (4). The eigenvalues illustrate at least two important conclusions about the effects of the values of K^* and k^*. First, the natural frequency increases when K^* and k^* are included as well as when the swirl ratio is increased. The variation of K^* in Figure 5 explains these observations. More importantly, the percent differences between the two models show that the values of K^* and k^* have very little effect on natural frequency. Second, stability is reduced when K^* and k^* are included and when the swirl ratio is increased. The variation of k^* in Figure 5 is the cause of these observations. Finally, the percent differences between the two models show that K^* and k^* can cause appreciable reductions in relative stability.

Table 4. Natural frequencies of free vibration for the pump model with and without K^* and k^*.

$\tilde{u}_{iL}$	$\frac{\omega_n}{\omega_s}$ with K^* and k^*	$\frac{\omega_n}{\omega_s}$ without K^* and k^*	percent decrease
.5	.747	.727	2.68%
.6	.777	.724	6.82%
.7	.800	.715	10.63%

To show that the stability and frequency of free vibration are determined only by the root obtained from the iterative approach described earlier, the equations of motion (9) were integrated in a series of transient, free-vibration simulations. Initial conditions were an initial displacement of .127 mm (.005 in) and velocity equal to $R_L\omega_s$ (synchronous whirl). Figure 8 includes the resulting orbit and a time history of the whirl frequency ratio for free vibration and an inlet swirl ratio of .7. As shown, the rotor executed a well-damped spiral

orbit. The whirl frequency ratio of the orbit was exactly .8, which corresponds to the natural frequency found earlier. The other two swirl ratios yielded similar results.

Table 5. Real parts of the eigenvalues for the model with and without K^* and k^*.

$\tilde{u}_{tL}$	real part with K^* and k^*	real part without K^* and k^*	percent decrease
--	1/sec	1/sec	--
.5	-55.9	-60.3	7.87%
.6	-31.1	-47.2	51.80%
.7	-13.8	-34.5	150.00%

To verify that the stability of the model is described only by the real part of the eigenvalues obtained with the iterative approach described above, the direct damping coefficient was reduced by 12.5% producing a range of unstable eigenvalues as shown in Figure 9 where the real part of the forward-whirl root is positive between whirl frequency ratios of .41 and .57. The natural frequency of this altered model corresponds to a stable eigenvalue and is $.825\omega_s$. Integration of the equations of motion showed that free vibration was indeed stable and occurred at the new natural frequency. In addition, the equations of motion were altered to include a harmonic forcing function with an amplitude of 5 N which forced the rotor in a circular direction at a frequency of $.5\omega_s$. Figure 10 includes the resulting orbit, whirl frequency ratio time history and a Fast Fourier Transform (FFT) of the x-coordinate, respectively. Even though the forcing frequency was within the unstable range of frequencies, the figures show that the system was stable in that its orbit did not grow without bound. The loops and limit cycle behavior are the results of the nonlinearities in the model. The FFT shows that the steady state orbit consisted of response at both the forcing frequency, $.5\omega_s$, and the natural frequency, $.825\omega_s$. Other forcing frequencies were also tried. Using a stable value of $.7\omega_s$, for example, the response did not behave in the same manner; instead, the orbit reached a steady state circular path at the excitation frequency as would be expected from a linear system. However, forcing at $.375\omega_s$, the characteristics of the results from forcing at $.5\omega_s$ occurred again, as can be seen in Figure 11, which again contains the orbit, time history of the whirl frequency ratio and an FFT of the response. Only forcing frequencies below and within the unstable zone resulted in this behavior. Only when the direct damping coefficient was reduced until the natural frequency corresponded to an unstable eigenvalue did the response become unstable in a linear sense, where the orbit grew without bound at the natural frequency. The fundamental result from this analysis is a verification that a range of whirl frequencies yielding eigenvalues with positive real parts does not cause the system response to grow without bound unless it includes the system natural frequency. In addition, the nonlinearities of the system can cause a limit cycle to occur under certain conditions.

Finally, the critical speed of the rotor can not be calculated unless force curves are available at other shaft speeds. In this case, the natural frequency is calculated with the iterative method just described, but at a number of shaft speeds. A plot of natural frequency as a function of shaft speed is then drawn, analogous to "critical speed maps" in fluid-film bearing analysis. The critical speed is defined as the speed where the natural frequency is equal to the shaft speed.

FREQUENCY RESPONSE

As discussed earlier, the following are the equations of motion of the model

$$\begin{bmatrix} M & 0 \\ 0 & M \end{bmatrix}\begin{Bmatrix} \ddot{x} \\ \ddot{y} \end{Bmatrix}+\begin{bmatrix} C & c \\ -c & C \end{bmatrix}\begin{Bmatrix} \dot{x} \\ \dot{y} \end{Bmatrix}+\begin{bmatrix} K(f) & k(f) \\ -k(f) & K(f) \end{bmatrix}\begin{Bmatrix} x \\ y \end{Bmatrix}=F\begin{Bmatrix} \cos\Omega t \\ \sin\Omega t \end{Bmatrix}, \tag{11}$$

where the right-hand side represents a harmonic forcing function appropriate to frequency response analyses. As in traditional methods, the transient solution is assumed to decay with time, and only the steady-state response of the rotor is considered. The forcing frequency is defined by Ω which has been used to represent whirl speed. Since the steady-state motion is assumed to occur at the same frequency as the excitation, this should not cause confusion. Note that the model is now linear because the whirl frequency ratio and, hence, the stiffnesses are constant. Multiplying the second equation by the complex number i, the equations can be combined into one in terms of the complex variable z.

$$M\ddot{z} + (C - ic)\dot{z} + (K - ik)z = Fe^{i\Omega t}. \tag{12}$$

Assuming steady-state motion of the following form

$$z = Re^{i\phi}, \tag{13}$$

where R denotes the whirl amplitude, and ϕ is the phase angle yields

$$\frac{R}{F/K} = \frac{K}{\sqrt{[K - M\Omega^2 + c\Omega]^2 + [C\Omega - k]^2}}$$

$$\phi = \tan^{-1}\left[\frac{k - C\Omega}{K - M\Omega^2 + c\Omega}\right]. \tag{14}$$

Equations (14) were solved using the present model data, and the results for a swirl ratio of .7 are shown in Figures 12 and 13. Also included are the same results for the model with K^* and k^* neglected. Again, in obtaining frequency response curves as shown in Figures 12 and 13, the stiffness terms must be calculated at the corresponding whirl frequency ratio.

The swirl ratio of .7, shown, exhibited the largest variation in amplitude and phase at the whirl frequency ratio of .80, the system natural frequency. An amplitude difference of about 60% is shown between the curves, suggesting that K^* and k^* have significant influence on the system primarily at this frequency. The swirl ratios of .6 and .5 exhibited similar but decreasing results in both the amplitude and phase curves, having differences in amplitude at the peak value of 35% and 6%, respectively. In fact, the curves were almost identical in the case corresponding to a swirl ratio of .5. Note that these resonance peaks occurred in all cases at the corresponding natural frequencies found in the previous section, further verifying the preceding results. The difference in the response to imbalance excitation between the two models is small, and this suggests that the leakage path forces have negligible effects at this frequency especially at low inlet swirl ratios. However, the presence of a subsynchronous excitation near the natural frequency can result in large increases in response amplitude when k^* is included. Finally, these results depend on the

choice of $\bar{C}$. The denominator of the first of equations (14) demonstrates that the amplitude increases as $C\Omega$ approaches k. Therefore, the observations stated above apply only for the damping values stated earlier.

SUMMARY AND CONCLUSIONS

The impeller-shroud forces have been separated into a.) constant (whirl frequency-independent) stiffness, damping and inertia coefficients and b.) direct and cross-coupled added stiffness coefficients which are functions of whirl frequency. With this approach, the model can be analyzed using traditional techniques with a few modifications. A new iterative technique was used in the determination of system stability and free vibration natural frequency. The whirl-frequency-dependent stiffness terms were seen to be convenient and effective models for the impeller-shroud force nonlinearities.

When the values of the added stiffness coefficients, K^* and k^*, were included in addition to the frequency-independent coefficients, a number of effects resulted. First, the natural frequency was seen to increase by a small amount, suggesting that K^* could be neglected when only the natural frequency is important. In addition, the stability is seen to decrease when k^* is included. This effect is appreciable, so stability calculations should include k^*. The frequency response analysis showed synchronous response to imbalance is increased by the stiffnesses although by only a small amount. Appreciable differences in response due to subsynchronous excitation occur only at or near the natural frequency and become negligible at low values of the inlet swirl ratio.

To find the natural frequency and stability of the system, a new iterative technique was used. The resulting eigenvalues were shown to completely describe the characteristics of free vibration. The nonlinearities in the model resulted in loop-filled orbits and limit cycles under specific conditions.

LIST OF SYMBOLS

$\tilde{C} = \frac{CQ_o\omega_s}{F_o}$	nondimensionalized direct damping coefficient
$\tilde{c} = \frac{cQ_o\omega_s}{F_o}$	nondimensionalized cross-coupled damping coefficient
$\tilde{F}_{r/t} = \frac{F_{r/t}}{F_o}$	nondimensionalized radial and tangential forces on the rotor
$F_o = 2R_L L\Delta P$	(Childs, 1987) (F)
$f = \frac{\Omega}{\omega_s}$	whirl frequency ratio
$\tilde{K} = \frac{KQ_o}{F_o}$	nondimensionalized direct stiffness coefficient
K^*	direct stiffness coefficient which is a function of the whirl frequency ratio (F/L)
$\tilde{k} = \frac{kQ_o}{F_o}$	nondimensionalized cross-coupled stiffness coefficient [19]
k^*	cross-coupled stiffness coefficient which is a function of the whirl frequency ratio (F/L)
L	length of seal or impeller-shroud path (L)
$\tilde{M} = \frac{MQ_o\omega_s^2}{F_o}$	nondimensionalized direct mass coefficient [19]
Q	rotor whirl radius (L)
Q_o	clearance at leakage path entrance (L)
$\tilde{q} = \frac{Q}{Q_o}$	clearance ratio
R	rotor whirl amplitude (L)
$R_{L,s}$	inlet radius of shroud leakage path or seal (L)
$\tilde{u}_{tL/s} = \frac{u_{tL/s}}{R_L\omega_s}$	nondimensionalized tangential fluid velocity at leakage path or seal entrance (inlet swirl ratio) [19]
x, y	rectangular coordinates of rotor center (L)
Z	complex rotor whirl amplitude (L)
$z = x + iy$	complex rotor coordinate (L)
ϕ	phase angle of whirl from harmonic excitation
Ω	rotor whirl frequency (1/T)
ω_n	natural frequency of free vibration (1/T)
ω_s	shaft speed (1/T)
L	shroud leakage path coefficient subscript
r	rotor coefficient subscript
s	seal coefficient subscript
sh	shaft coefficient subscript
none	overall coefficient subscript

REFERENCES

Adtkins, D., 1976, "Analyses of Hydrodynamic Forces on Centrifugal Pump Impellers," M. S. Thesis, California Institute of Technology, Pasadena.

Bolleter, U., Wyss, A., Welte, I. and Sturchler, R., 1985, "Measurements of Hydrodynamic Interaction Matrices of Boiler Feed Pump Impellers," ASME, Paper No. 85-DET-148.

Childs, D., Dressman, J. and Childs, S., 1980,."Testing of Turbulent Seals for Rotordynamic Coefficients," Proc. of Workshop on Rotordyn, Inst. Prob. in High-Perf. Turbomach., Texas A&M University, NASA CP-2133, pp. 121-38.

Childs, D., 1981, "Convergent-Tapered Annular Seals: Analysis for Rotordynamic Coefficients," Symp. Vol., Fluid/Structure Interactions Turbomach., ASME Winter Annual Meeting, pp. 35-44.

Childs, D., 1982a, "Dynamic Analysis of Turbulent Annular Seals Based on Hirs' Lubrication Equations," ASME Paper No. 82-Lub-41.

Childs, D., 1982b, "Finite-Length Solutions for Rotordynamic Coefficients of Turbulent Annular Seals," ASME Paper No. 82-Lub-42.

Childs, D. and Dressman, J., 1982c, "Testing of Turbulent Seals for Rotordynamic Coefficients," Proc. of Workshop on Rotordyn. Inst. Prob. in High-Perf. Turbomach., Texas A&M University, NASA CP-2250, pp. 157-71.

Childs, D. and Moyer, D., 1985, "Vibration Characteristics of the HPOTP (High Pressure Oxygen Turbopump) of the SSME (Space Shuttle Main Engine),"ASME Trans. Journ. of Eng. for Gas Turbine, and Power, 107, pp. 152-59.

Childs, D., 1987, "Fluid-Structure Interaction Forces At Pump-Impeller-Shroud Surfaces For Rotordynamic Calculations," Texas A&M University, Mech. Engr. Dept., accepted for presentation at ASME Vibration Conference, Boston, Mass.

Franz, R. and Arndt, N., 1986, "Measurement of Hydrodynamic Forces on the Impeller of the SSME," Report No. E249.2, California Institute of Technology, Pasadena.

Jeffcott, H., 1919, "The Lateral Vibration of Loaded Shafts in the Neighborhood of a Whirling Speed - The Effect of Want of Balance," The Philosophical Magazine, 6(37), pp. 304-14.

Jery, B., Acosta, J., Brennen, C. and Caughey, T., 1984, "Hydrodynamic Impeller Stiffness, Damping and Inertia In the Rotordynamics of Centrifugal Flow Pumps," Proc. of Workshop on Rotordyn. Inst. Prob. in High-Perf. Turbomach., Texas A&M University, NASA CP-2338, pp. 137-60.

Massey, I. C., 1985, "Subsynchronous Vibration Problems in High Speed Multistage Centrifugal Pumps," Proc. of the 14th Turbomach. Symposium, Turbomachinery Laboratories, Texas A&M University, pp. 11-16.

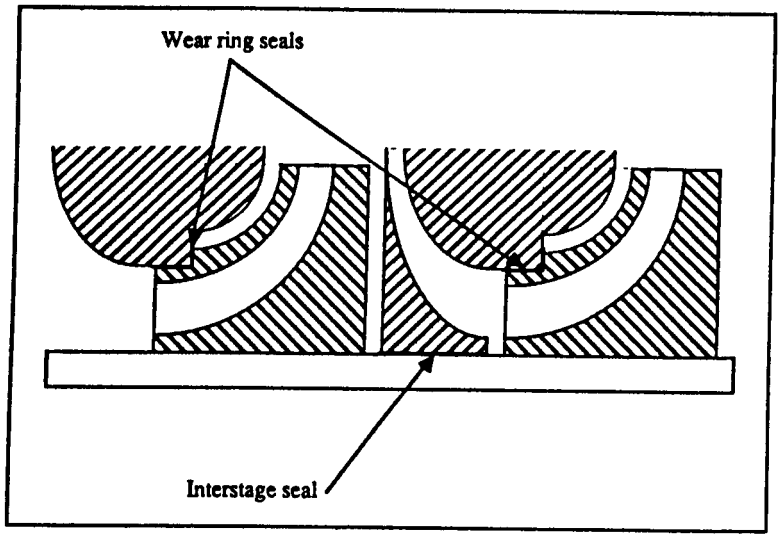

Figure 1. Typical seal configurations for a multi-stage pump.

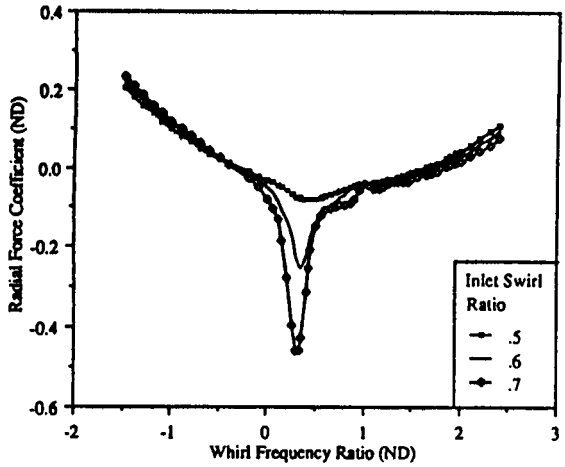

Figure 2a. Radial force coefficient curves (Childs, 1987).

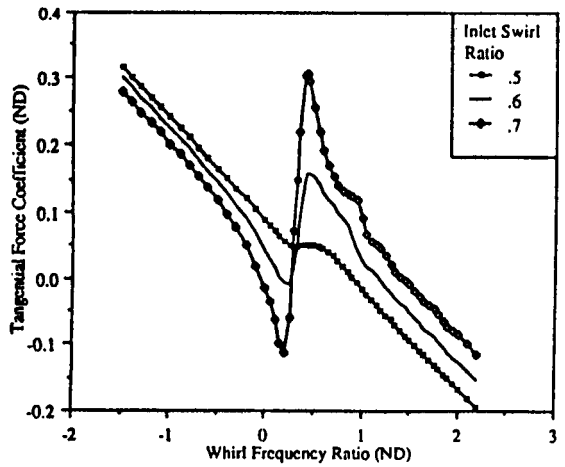

Figure 2b. Tangential force coefficient curves (Childs, 1987).

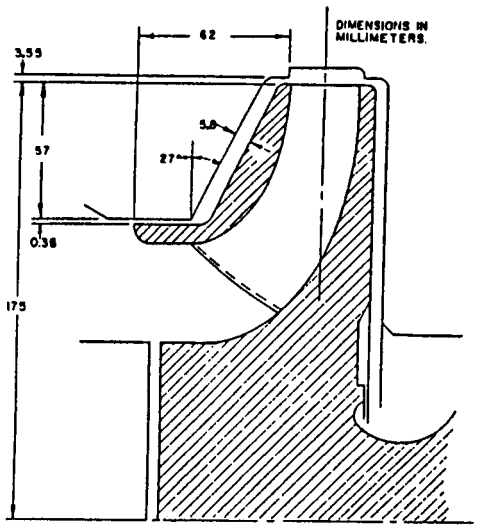

Pump data

shaft speed = ω_s = 2000 rpm

inlet clearance = Q_o = 3.55 mm

impeller exit angle = 22.5 °

flowrate = 130 l/sec

head developed = 68 m

seven-bladed impeller

working fluid is water at 80 °F

Figure 3. Dimensions and data for the pump tested by Bolleter et al. (Bolleter, et al., 1985).

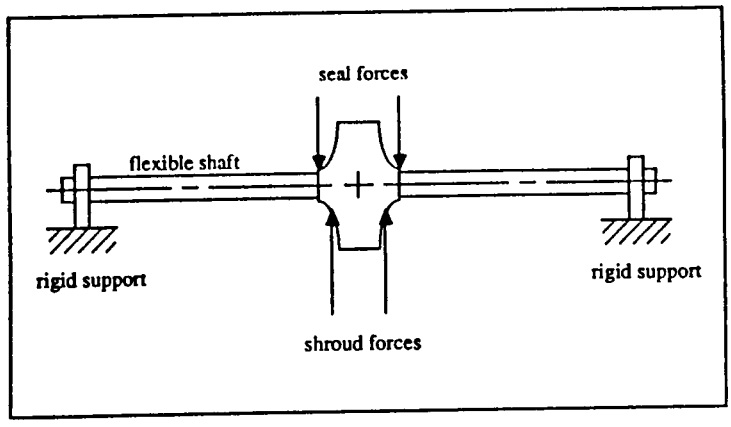

Figure 4. Jeffcott-based, double-suction impeller leakage path model.

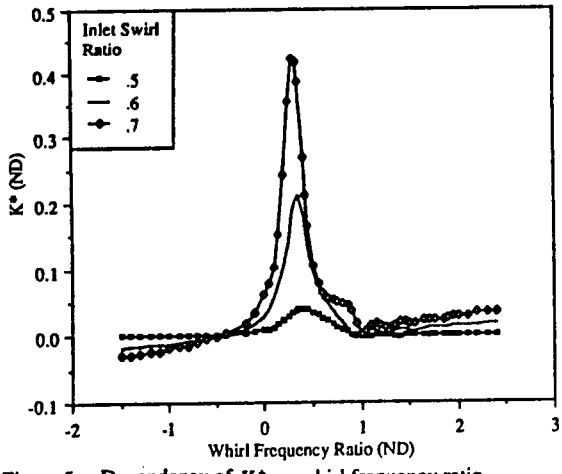

Figure 5a. Dependency of K* on whirl frequency ratio.

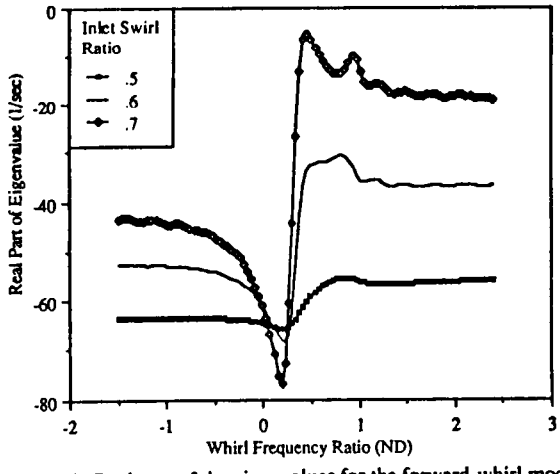

Figure 6. Real part of the eigenvalues for the forward-whirl mode.

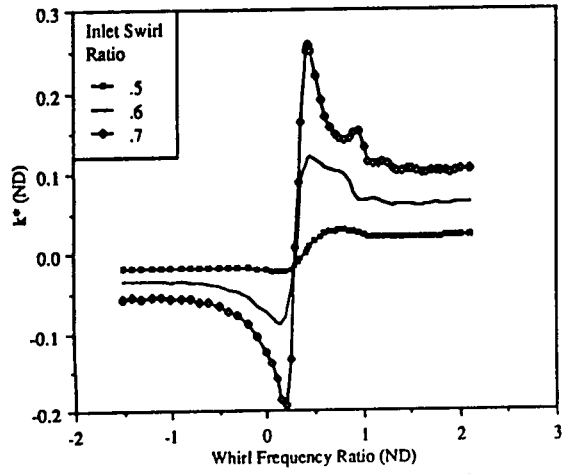

Figure 5b. Dependency of k* on whirl frequency ratio.

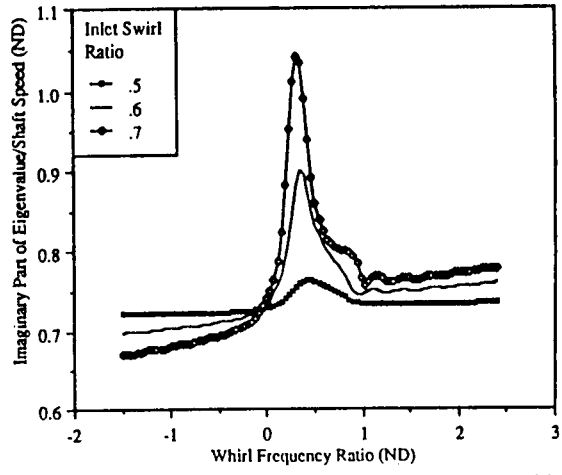

Figure 7. Imaginary part of the eigenvalues for the forward-whirl mode.

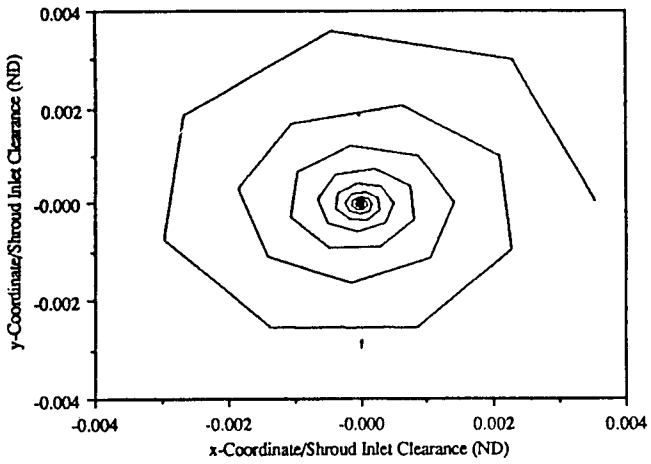

Figure 8a. Rotor orbit during free vibration.

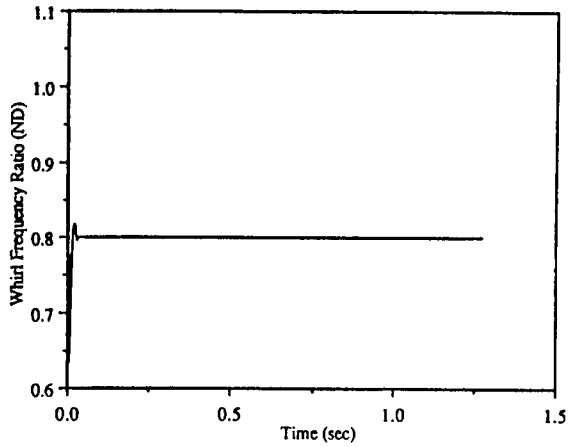

Figure 8b. Time history of rotor whirl frequency ratio during free vibration.

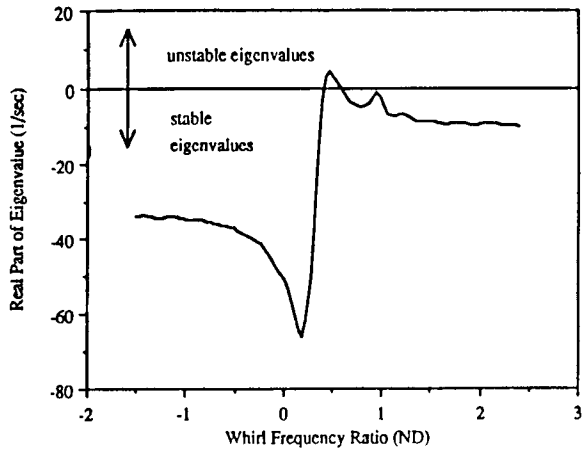

Figure 9. Real part of the eigenvalues for the forward-whirl mode with a 12.5% reduction in direct damping.

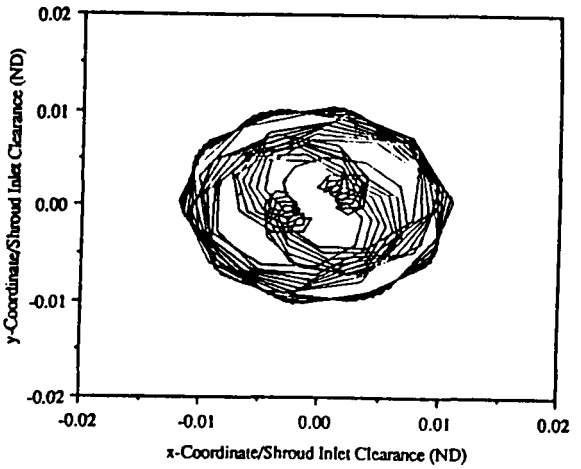

Figure 10a. Rotor orbit during harmonic excitation at 50% of shaft speed and 12.5% reduction in direct damping.

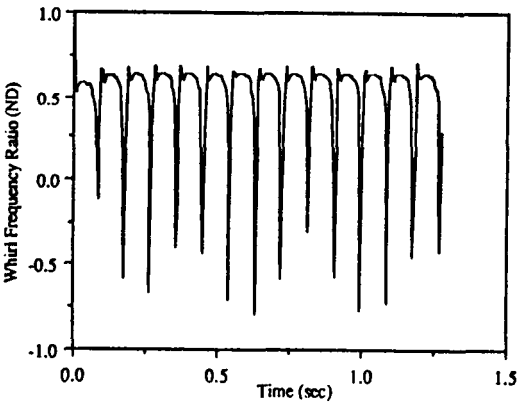

Figure 10b. Time history of rotor whirl frequency ratio during harmonic excitation at 50% of shaft speed and a 12.5% reduction in direct damping.

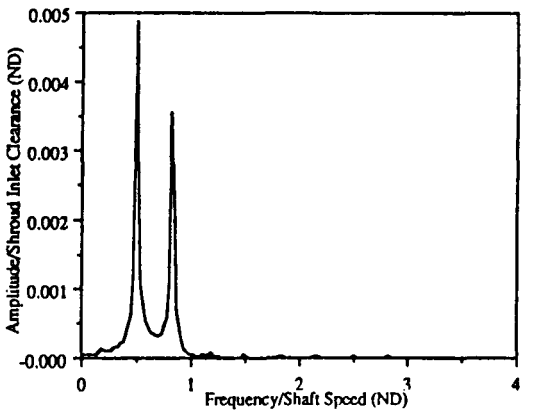

Figure 10c. FFT of the response of the rotor during harmonic excitation at 50% of shaft speed and a 12.5% reduction in direct damping.

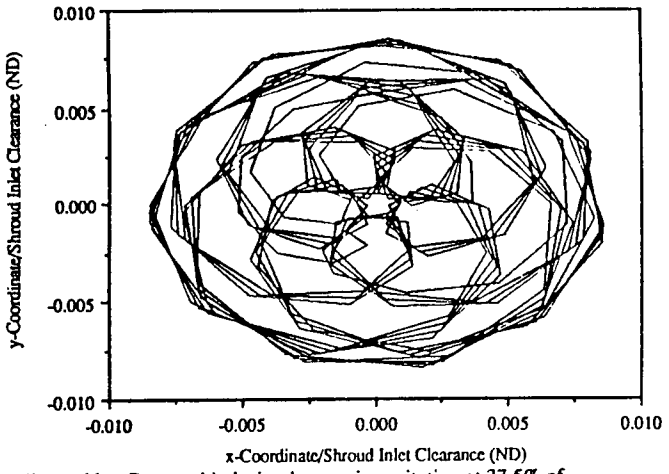

Figure 11a. Rotor orbit during harmonic excitation at 37.5% of shaft speed and a 12.5% reduction in direct damping.

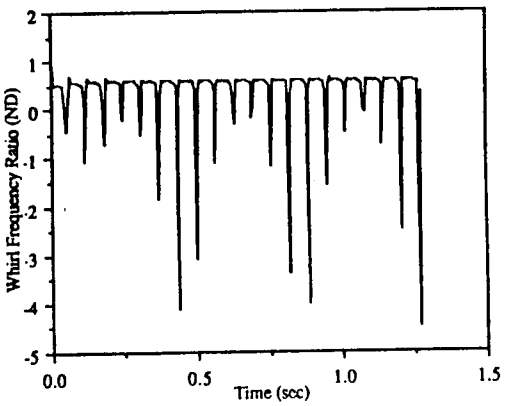

Figure 11b. Time history of rotor whirl frequency ratio during harmonic excitation at 37.5% of shaft speed and a 12.5% reduction in direct damping.

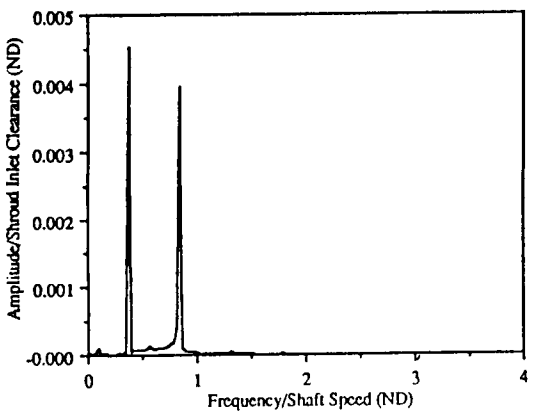

Figure 11c. FFT of the response of the rotor during harmonic excitation at 37.5% of shaft speed and a 12.5% reduction in direct damping.

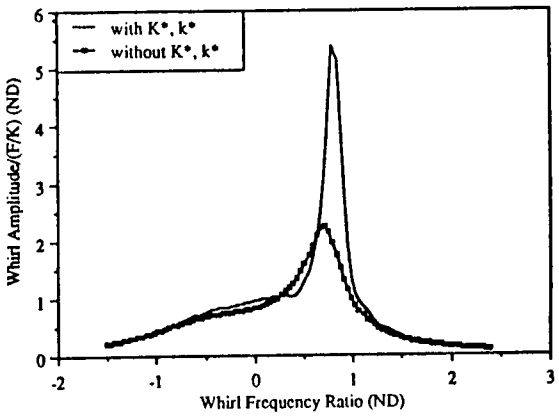

Figure 12. Frequency response: whirl amplitude.

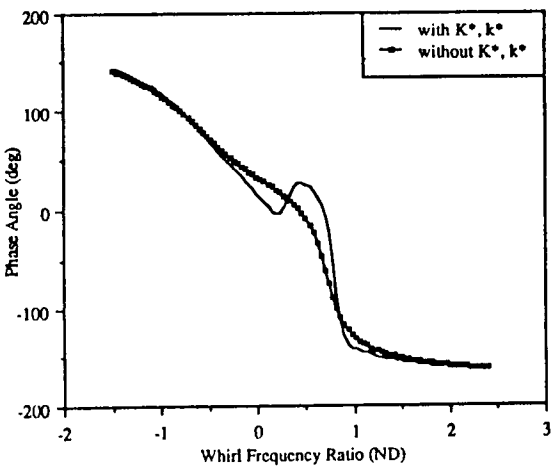

Figure 13. Frequency response: phase angle.